RESEARCH PAPER

CrossMark

Residual stress evaluation of components produced via direct metal laser sintering

Brandon Kemerling[1] · John C. Lippold[1] · Chris M. Fancher[2] · Jeffrey Bunn[2]

Abstract

Direct metal laser sintering is an additive manufacturing process which is capable of fabricating three-dimensional components using a laser energy source and metal powder particles. Despite the numerous benefits offered by this technology, the process maturity is low with respect to traditional subtractive manufacturing methods. Relationships between key processing parameters and final part properties are generally lacking and require further development. In this study, residual stresses were evaluated as a function of key process variables. The variables evaluated included laser scan strategy and build plate preheat temperature. Residual stresses were measured experimentally via neutron diffraction and computationally via finite element analysis. Good agreement was shown between the experimental and computational results. Results showed variations in the residual stress profile as a function of laser scan strategy. Compressive stresses were dominant along the build height (z) direction, and tensile stresses were dominant in the x and y directions. Build plate preheating was shown to be an effective method for alleviating residual stress due to the reduction in thermal gradient.

Keywords Additive manufacturing · Direct metal laser sintering · Residual stress · Neutron diffraction · SYSWELD

1 Introduction

Direct metal laser sintering (DMLS) is an additive manufacturing (AM) process which allows for the direct fabrication of three-dimensional components. Computer-aided

✉ Brandon Kemerling
  kemerling.5@osu.edu

[1] Welding Engineering Program, Department of Materials Science and Engineering, The Ohio State University, Columbus, OH, USA

[2] Neutron Scattering Division, Oak Ridge National Laboratory, Oak Ridge, TN, USA

design (CAD) software is used to design and generate digital data for the component geometry. The data is then used as an input to the AM machine to guide the process. Components are built in a layer-by-layer fashion utilizing a laser energy source, build plate, and metal powder particles. A schematic of the process is shown in Fig. 1. A thin layer of powder particles is spread with a blade or roller from the powder reservoir to the top of the build plate region. The laser then selectively melts regions of the powder layer according to the component design. Upon solidification of the melted region, a dense layer of the component is created. The build plate is then lowered by a distance equal to the layer thickness and a fresh layer of powder is delivered. The laser again melts the powder and fuses the new layer to the preceding layer. These steps are repeated on the order of hundreds to thousands of times until the desired parts are complete. Once completed, the build plate is removed from the machine along with the attached parts. The remaining unfused powder is also removed and commonly recycled. The entire process takes place within an enclosed build chamber under inert atmosphere to avoid oxidation.

DMLS offers several advantages with respect to traditional subtractive manufacturing methods. It eliminates requirements for complex tooling and molds, which allows for
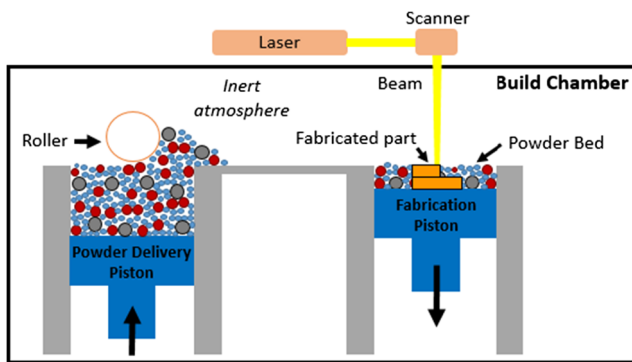
Fig. 1 Schematic of the direct metal laser sintering process

unmatched freedom in component design [1]. The ability to create complex parts with internal cavities and lattice structures, otherwise unachievable, has already been demonstrated [2–5]. Component customization is also easily achievable by simply modifying the input CAD file. This, in turn, makes the production of one-off, customized components economically viable [6]. Material waste reductions can also be realized, as buy-to-fly ratios (the ratio between raw material used and final part weight) for aerospace components have been reduced from 33:1 to nearly 1:1 [7]. These key advantages have led to the implementation of DMLS processing in the aerospace, automotive, and biomedical industries [8]. Materials used have included steels, stainless steels, titanium, nickel, and aluminum-based alloys [9].

Although DMLS offers several advantages, the process is relatively immature with respect to traditional manufacturing technologies. Relationships between key processing parameters and final part properties are still lacking and require further development. Specifically, strategies for controlling residual stress accumulation are of interest. Residual stresses, which are stresses remaining in a material when external loading forces have been removed, are known to be prevalent in DMLS builds [10, 11]. They accumulate due to the localized heating and cooling thermal cycles imposed by the laser energy source, which generates thermal gradients near the melt pool. This results in the non-equilibrium expansion and contraction of material in the immediate vicinity of the melt pool and in underlying build layers. The spatial competition between material expansion and contraction at elevated temperature ultimately results in the accumulation of residual stress upon cooling to room temperature.

Controlling residual stress during DMLS processing is important to avoid undesirable build outcomes. Residual stresses can lead to issues involving part distortion, interlayer delamination, and cracking, which eventually result in build failure [12]. Residual stresses may also influence the mechanical properties and corrosion resistance of parts successfully built using DMLS [13, 14]. In some instances, post build heat treatments applied to relieve residual stresses can lead to undesirable part distortion [15].

Common techniques for residual stress measurement can be categorized as destructive or nondestructive. Destructive tests involve measuring stress relief as free surfaces are generated in a sample of interest. This often involves the use of strain gauges or digital image correlation to measure deformation as the sample is locally relieved of stresses by sectioning or hole drilling. Destructive evaluation methods obviously result in permanent damage to the tested sample. Common nondestructive test methods involve the use of X-ray or neutron diffraction to accurately measure near-surface and volumetric residual stresses, respectively. Although nondestructive test methods require the use of specialized equipment, the measurement accuracy and ability to preserve component integrity make the use of nondestructive test methods preferable [16].

Previous research has been conducted to evaluate residual stresses as a function of DMLS process variables. It is well documented that stress values can vary significantly depending on the overall build strategy employed. Variables that have been explored include energy input, layer thickness, and laser scan strategy [10, 11, 17]. The influence of support structures and post-processing heat treatments on residual stress levels have also been investigated [4, 18]. Additionally, comparisons of residual stresses between DMLS and other metal AM processes have been reported [19]. A comprehensive review of these efforts can be found elsewhere [20].

For welding applications, preheating is a technique commonly employed to reduce residual stress presence [21]. Techniques for applying preheat treatments may involve weld exposure to furnaces, electrical strip heaters, or induction and radiant heaters. Since welding processes use a localized high-temperature heat source, a steep thermal gradient exists between the heat source and surrounding base material. Preheating acts to reduce the thermal gradient by raising the temperature of the surrounding base material. This reduction in thermal gradient partially alleviates the non-equilibrium expansion and contraction of material which occurs as a function of temperature and thus location in the weld region. As a result, reductions in residual stress accumulation upon cooling to room temperature can be realized. Preheating has been shown to be an effective method for reducing residual stresses in welding-related studies [21, 22]. However, further investigations are required to evaluate the influence of preheating on residual stress presence in DMLS applications.

In this study, the influence of laser scan strategy on residual stress presence in DMLS builds made with 304L stainless steel was evaluated. Specifically, a stripe scan strategy was applied using two different approaches. Experimental residual stress measurements were made via neutron diffraction. A finite element model was also developed and validated with experimental results. The model was used to evaluate a method for minimizing residual stress levels, which was achieved through build plate preheating throughout the duration of the simulated DMLS builds.

2 Materials and procedure

2.1 Materials

304L stainless steel powder from Carpenter Powder Products (CPP) was used as the input material. The powder was produced via gas atomization with argon. Figure 2 provides an SEM image of the powder particles. The particles were found to be spherical, which is expected of powder produced via gas atomization [23]. The particle size distribution was measured via laser diffraction with a HORIBA Scientific CAMSIZER XT system. The particle size distribution is presented in Table 1. D10, D50, and D90 values are included to quantify the size distribution. The D10 value of 20.8 μm indicates that 10% of the powder particles are smaller than 20.8 μm. Likewise, D50 and D90 refer to the respective values of 50 and 90%. Table 2 provides the chemical composition of the input powder, as provided by CPP. Virgin powder was used for each build in order to avoid the additional variables associated with recycled powder.

The build plate material used was also 304L stainless steel. The dimensions of the plate were 75 mm × 125 mm with a thickness of 10 mm. Surface grinding of the plate reduced the laser reflectivity during the processing of initial build layers.

2.2 Experimental build procedure

An EOSINT M 280 machine was used to fabricate components via DMLS. The machine was equipped with a 400-W Yb-fiber laser and argon gas was pumped into the build chamber to create an inert environment. To develop optimal processing parameters, a design of experiment was carried out. The parameters which were varied included laser power, laser
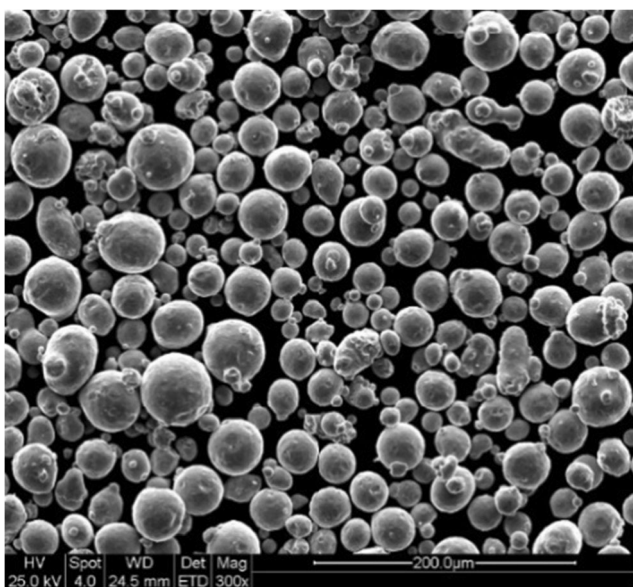

Fig. 2 SEM image of gas-atomized 304L powder particles

Table 1 Powder particle size distribution

Powder size characteristic	Value
D10 (μm)	20.8
D50 (μm)	31.2
D90 (μm)	46.3
Mean (μm)	32.6

scan speed, and layer thickness. Simple prisms were built and evaluated for their density in the as-built condition. This was conducted by preparing metallographic samples using standard techniques [24]. The density of each sample was then evaluated using optical microscopy in conjunction with ImageJ image analysis software [25]. The parameter set which yielded the highest density value (99.7%) was adopted for component builds. The parameters are provided in Table 3.

Microstructural analysis was conducted following electrolytic etching with 10% oxalic acid at 5 V and 1 A for approximately 20 s. Figure 3 provides micrographs of the etched samples. The build layer boundaries and fusion boundaries from individual laser scans can be clearly seen. Epitaxial growth of cellular dendrites was also observed, as solidification initiated at the fusion boundaries between layers. Primary dendrite arm spacing was in the range from 1 to 3 μm. This fine spacing results from the rapid cooling rates associated with laser processing. Electron backscatter diffraction (EBSD) was also used to evaluate the grain structure. EBSD scan data was analyzed and mapped with EDAX OIM software. Figure 4a displays a unique grain map and Fig. 4b provides an inverse pole figure. The grain size was consistent throughout the sample and was on the order of 21 μm on average. Significant texture was not present in the sample, as the grains were observed to be randomly oriented from the inverse pole figure.

The component geometry used for residual stress evaluation is presented in Fig. 5. The geometry was developed as part of a standard weldability testing procedure for DMLS applications. The geometry consists of two Block-Os joined by eight connection regions. The dimensions of the component are 25.6 mm × 33.2 mm, with a build height of 10 mm. Two hundred fifty individual layers were used for fabrication. The components were built directly on the build plate without the use of support structures. Preheating was not applied to the build plate.

Two components were fabricated with variations in the laser scan strategy. Figure 6a presents the applied scan strategies. The first component was built using an "edge to edge" approach. The laser scan initiated at an edge of the sample and was simply translated across the layer to the opposite edge. The second component was built using a "perimeter first" approach. The perimeter of the component was scanned first and was immediately followed by scanning of the interior Block-O. The connecting regions were then built to complete an individual layer. Although the regions of each component

Table 2 Chemical composition of 304L input powder

Element	Fe	Cr	Ni	Mn	Si	N	O	C	P	S
Wt%	Bal	18.4	9.8	1.5	0.53	0.05	0.019	0.015	0.012	0.003

were built in a different sequence, the laser scanned in a stripe pattern to complete each region. The stripe pattern is shown in Fig. 6b. The width and length of each stripe was 0.1 and 10 mm, respectively. Adjacent stripes did not overlap. The orientation of the stripes was rotated 67° for each subsequent layer. Following component fabrication, wire electrical discharge machining (EDM) was used to cut the components into individual sections. This was to aid in sample alignment for neutron diffraction. The components were not removed from the build plate.

Figure 6c shows the two fabricated components as well as the two reference cubes. The cubes were fabricated using the process parameters presented in Table 3. They were then removed from the build plate via wire EDM prior to neutron diffraction analysis. The purpose of the reference cubes is described in Section 2.3.

2.3 Neutron diffraction

Residual strain measurements were taken on the HB-2B beam line at the High Flux Isotope Reactor's (HFIR) Neutron Residual Stress Mapping Facility (NRSF2) at Oak Ridge National Laboratory (ORNL). A total of four builds were evaluated: two components produced with differences in laser scan strategy and two reference cubes. Each sample was aligned with the beam line, initially using a distance-measuring theodolite and subsequently by incrementally translating each sample through the beam on a motorized stage to precisely locate the sample edges. Care was taken to ensure proper sample alignment, as this is a critical step for collecting accurate data [26, 27]. As the neutron beam was diffracted from each sample, seven linear position-sensitive detectors were used to capture the scattered neutrons. The detectors were stacked vertically, and the top and bottom detectors spanned 17° out of the horizontal scattering plane.

In strain scanning, the gauge volume is defined by the intersection between the incident and scattered neutron beams. The gauge volume is commonly cubic, and the location of the

Table 3 DMLS processing parameters used

Process parameter	Value
Laser spot size (mm)	0.1
Laser power (W)	275
Scan speed (mm/s)	1100
Hatch size (mm)	0.1
Layer thickness (μm)	40

gauge volume within the sample of interest determines the location of strain measurement. The gauge volume location is thus "translated" within the sample to measure residual strain in various locations. The size of the gauge volume is selected by the user and is an important step to consider. The selection of a larger gauge volume size offers the advantage of reducing the time required to obtain data. However, a smaller gauge volume size offers finer spatial resolution for data acquisition. A balance between these considerations is often desired. Additional factors which influence the gauge volume size include grain size and texture. A sufficient number of randomly oriented grains within the gauge volume is required for accurate data collection [19]. Based on these considerations and the EBSD data presented in Fig. 4, the gauge volume size was set to 1 mm^3. This was controlled by placing 1 mm × 1 mm slits in the path of the incident neutron beam.

Residual strain was determined through Bragg's law by measuring distances between crystallographic planes of strained samples. Bragg's law is shown in Eq. 1, where λ is wavelength, d_{hkl} is lattice spacing, and θ is the diffraction angle.

$$\lambda = 2d_{hkl}\sin\theta \tag{1}$$

A silicon monochromator with {422} planes was used, which diffracted neutrons with a fixed wavelength (λ) equal to 1.537 Å. For 304L stainless steel, the {311} planes were selected to provide the peak scattering data. These planes were known to nominally scatter the neutrons at a 2θ angle equal to 90.5° with respect to the incident beam. To satisfy Bragg's law, any measured variation in 2θ is indicative of a change in the lattice spacing, d_{hkl}. Actual 2θ measurements were captured by the array of seven detectors spanning ± 17° out of the horizontal scattering plane. For each measurement, the detectors captured data for times ranging from 10 to 180 min. This time varied as a function of gauge volume location within the sample.

For each gauge volume location, d_{hkl} measurements were taken in the orthogonal x, y, and z directions. Shear strains were assumed to be negligible and were not measured [19]. To calculate residual strain, which is the change in lattice spacing with respect to the nominal lattice spacing (d_{hkl^0}), Eq. 2 was utilized.
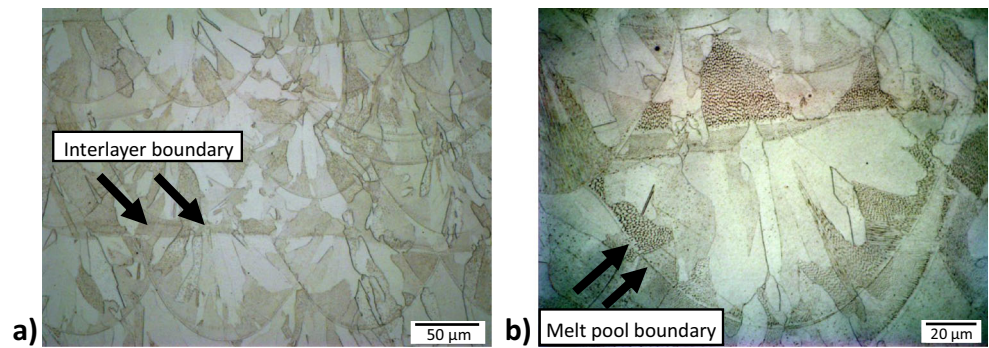
$$\varepsilon_{hkl} = \frac{d_{hkl} - d_{hkl^0}}{d_{hkl^0}} \tag{2}$$

As shown in Eq. 2, residual strain results are sensitive to the d_{hkl^0} parameter. One option for obtaining d_{hkl^0} is to measure the

Fig. 3 Microstructure of type 304L builds showing **a** an interlayer boundary and **b** melt pool boundary

lattice spacing of an input powder sample. However, this does not account for the microstructural or chemical composition differences introduced during DMLS processing. Therefore, a method has been developed to measure d_{hkl^0} from small cubes that have been fabricated by DMLS. This method is the most accurate and addresses microstructural and chemical composition changes introduced during DMLS processing [28–30].

d_{hkl^0} was obtained through lattice spacing measurement of strain-free reference cubes. The reference cubes were fabricated using DMLS and had dimensions of 5 mm × 5 mm × 5 mm. The cubes are shown in Fig. 6c. Prior to lattice spacing measurement, the cubes were removed from the build plate via wire EDM in order to mechanically relieve any residual stresses present. Due to their proximity to the other components on the build plate, it can be assumed that the cubes have the same microstructure and chemical composition gradient (if present) as the other components built.

Residual stresses were calculated using Hooke's law, shown in Eqs. 3–5. σ_{11}, σ_{22}, and σ_{33} are the residual stress values in the orthogonal x, y, and z directions, respectively. ε_{11}, ε_{22}, and ε_{33} are the residual strain components in the respective x, y, and z directions, as calculated from Eq. 2. The diffraction elastic constants for the {311} planes of 304L stainless steel were Young's modulus (E) and Poisson's ratio (v) values of 184 GPa and 0.29, respectively [31, 32].

$$\sigma_{11} = \frac{E}{(1+v)(1-2v)}\left[\varepsilon_{11}(1-v) + v(\varepsilon_{22} + \varepsilon_{33})\right] \quad (3)$$

$$\sigma_{22} = \frac{E}{(1+v)(1-2v)}\left[\varepsilon_{22}(1-v) + v(\varepsilon_{11} + \varepsilon_{33})\right] \quad (4)$$

$$\sigma_{33} = \frac{E}{(1+v)(1-2v)}\left[\varepsilon_{33}(1-v) + v(\varepsilon_{11} + \varepsilon_{22})\right] \quad (5)$$

Standard errors associated with the residual stress values were calculated and are presented as error bars in conjunction with the experimental results. The errors were obtained by propagating the errors measured in 2θ and d_{hkl^0} through Eqs. 1–5. The variation in 2θ was evaluated by the NRSF2 peak fitting program. Variance in d_{hkl^0} was obtained by replicating measurements on the strain-free reference cubes.

Figure 7 illustrates the locations of residual strain measurement within the component geometry. The red line shown in Fig. 7a indicates the plane on which measurements were recorded. Figure 7b provides a transparent image of the component in order to show the plane extends through the height of the component. This plane is shown in an alternative orientation in Fig. 7c. The two columns of white boxes displayed in Fig. 7b, c indicate the precise locations of residual strain measurement. The columns are labeled "inner" and "outer" for reference. The columns are aligned at each interface between the Block-Os and connection region. The gauge volume was translated within the component to the locations indicated by each individual white box. A total of 18 locations were evaluated. In each location, three measurements were recorded to obtain the x, y, and z directional strain values. The components

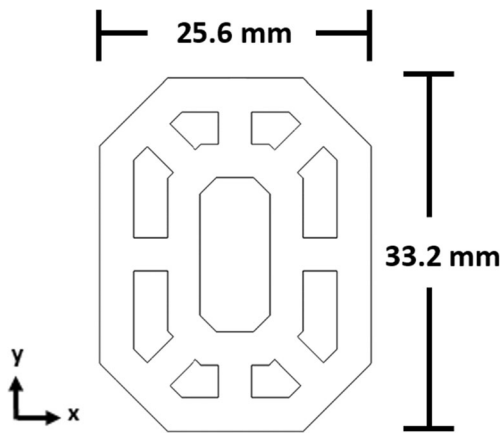**Fig. 4** EBSD maps showing **a** unique grain map and **b** inverse pole figure
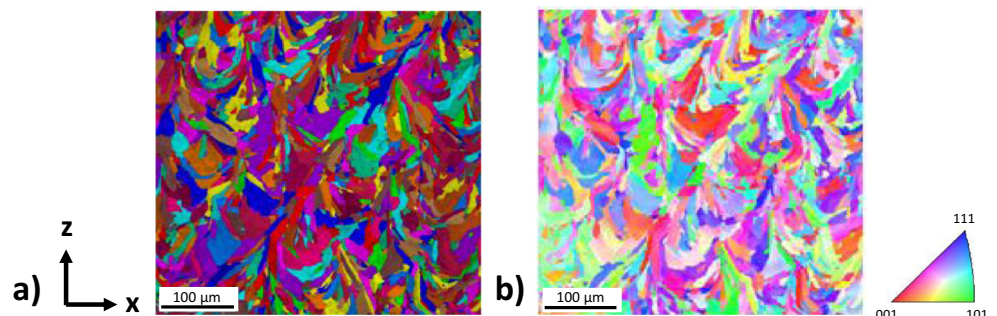
Fig. 5 Component geometry and dimensions

were rotated on the motorized stage to measure strain in the orthogonal x, y, and z directions.

2.4 Numerical simulation

Three-dimensional numerical simulations were developed through finite element analysis (FEA) to model the DMLS component build procedure. Three software packages were used to complete the simulations. Computer-aided design (CAD) software, SOLIDWORKS, was used to create the three-dimensional component file. This file included both the component and build plate. The generated file was then imported into ABAQUS to create an appropriate mesh for FEA. One hundred eighty six thousand twenty elements and 179,998 nodes were generated. The element size was nonuniform and varied as a function of location within the design file. A relatively fine element size was applied to the DMLS component build region and heat-affected zone of the build plate. A relatively coarse element size was applied to the remainder of the build plate. This consideration was made to reduce the overall computation time [33]. Following mesh generation, the file was imported into SYSWELD to simulate the DMLS build procedure.

The laser scan strategy was defined by sequentially selecting nodes within the component. A Gaussian heat flux distribution was then applied along the scan lines to simulate

laser processing. The heat flux distribution is presented in Fig. 8 and was defined by Eqs. 6–8.

$$F = Q_0 * e^{\left(-\frac{r^2}{r_0^2}\right)} \tag{6}$$

$$r = \left(x^2 + y^2\right)^{1/2} \tag{7}$$

$$r_0 = r_e - (r_e - r_i) * (z_e - z)/(z_e - z_i) \tag{8}$$

F is the source intensity, Q_0 is the maximum source intensity, r_e is the keyhole top radius at $z = z_e$, and r_i is the keyhole bottom radius at $z = z_i$. The depth of the laser penetration was set to one and a half times the individual layer thickness.

The simulation parameters followed the experimental parameters reported in Table 3. The absorbed energy was defined as 70% of the incident laser-supplied energy due to partial reflection from the powder bed [34]. Rigid boundary conditions were applied to the x, y, and z directions of the build plate region to simulate the experimental clamping conditions. As the build plate is secured in the DMLS machine with four bolts, the build plate is restrained from movement. Rigid boundary conditions were not applied to the DMLS build region. In addition, symmetry boundary conditions were not utilized for the model.

Convection and radiation cooling conditions were applied to the upper surface of the DMLS build component. Equations governing the convective and radiative cooling conditions are presented in Eqs. 9 and 10 respectively, where h is the convective heat transfer coefficient of air = 15 W/m^2 K, T is the surface temperature, T_0 is the ambient temperature = 20 °C, ε is the emissivity of 304L stainless steel = 0.8, and σ is the Stefan-Boltzmann constant = 5.67×10^{-8} W/m^2 K^4. Following the build procedure, the component was allowed to cool to room temperature via conductive, convective, and radiative heat transfer.

$$q_c = h(T - T_0) \tag{9}$$

$$q_r = \varepsilon\sigma\left(T^4 - T_0^4\right) \tag{10}$$

The simulation used an element activation and deactivation method to model the layer-by-layer addition of material to the
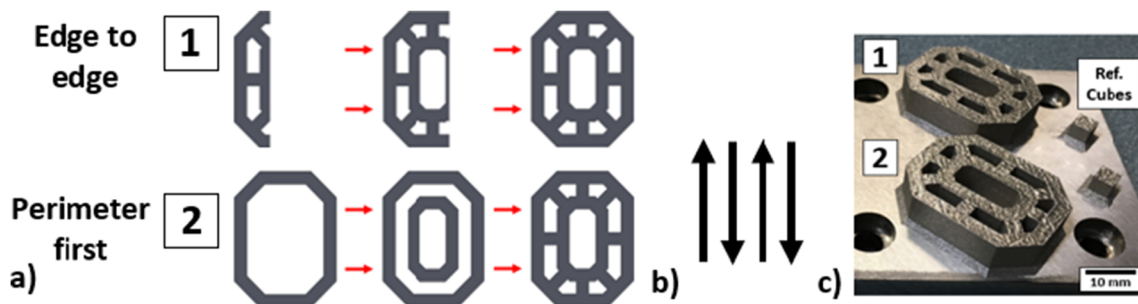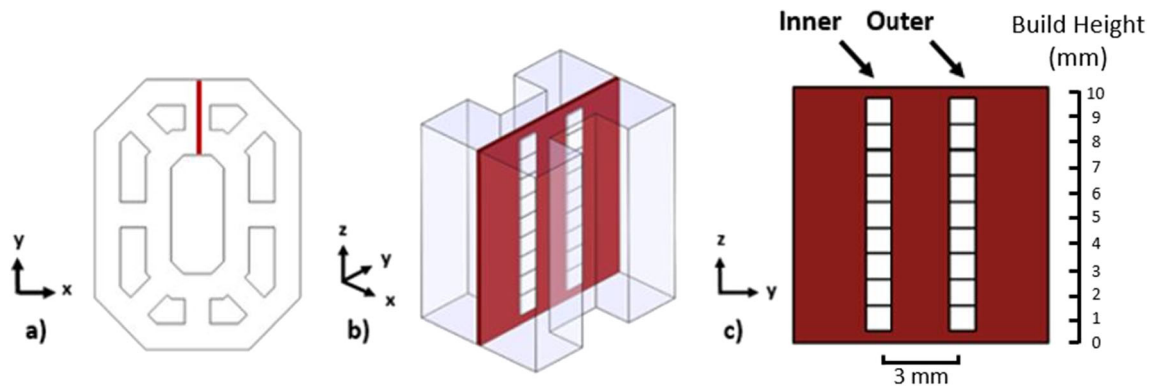

Fig. 6 **a** Laser scan strategies utilized. **b** Laser raster pattern. **c** Image of experimental build components

Fig. 7 **a** Location selected for neutron diffraction measurements (red line). **b** Plane of neutron diffraction measurements through component height. **c** Plane reoriented to show precise location of residual stress measurements (white boxes) in two separate columns

component. Although each element was created prior to simulation, the elements within the component build are deactivated until the laser scans within their immediate vicinity. As the laser scans along the defined paths, the local elements become activated, thereby modeling the gradual addition of material to the component.

The 304L material properties were defined as a function of temperature for the numerical simulation. Key properties including thermal conductivity, specific heat, and Young's modulus are presented in Fig. 9 as a function of temperature. These material properties were obtained from the SYSWELD material database V12.0. Poisson's ratio, coefficient of thermal expansion, and density were assumed to be constant as a function of temperature and were 0.29, 1.96×10^{-5}, and 7.72 g/cm^3, respectively. The latent heat of fusion value for 304L stainless steel was equal to 260 kJ/kg.

Figure 10 provides an image of the SYSWELD build simulation. The meshed elements, temperature profile, and laser-generated melt pool are shown. Simulations were run on a single core on a computer equipped with 16 GB of RAM. The average file size and time required to complete each simulation was 150 GB and 15 h, respectively.
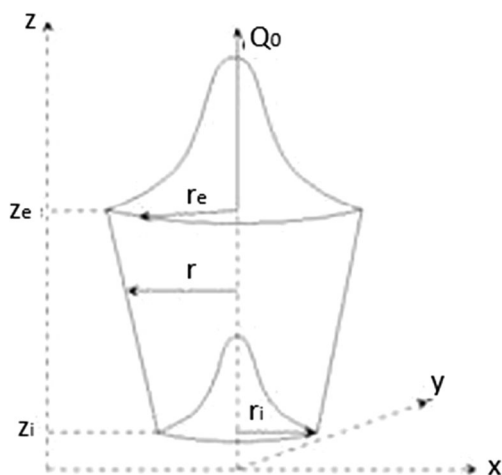
**Fig. 8** Gaussian heat distribution employed for laser processing [43]

The goal of the numerical simulations was to first develop a model which could be validated by experimental results. Following the model development, simulations were conducted to evaluate build plate preheating as a method for reducing residual stress presence within the DMLS component. The simulation was evaluated with build plate preheating temperatures of room temperature, 50, 100, 150, 200, and 250 °C. These preheat temperatures were maintained throughout the duration of the DMLS simulations.

3 Results and discussion

3.1 Neutron diffraction results

Residual strain and residual stress values were calculated using the procedure described in Section 2.3. Residual stresses were evaluated in the orthogonal x, y, and z directions as a function of the component build height. Additionally, the influence of laser scan strategy on residual stress presence was evaluated. Figure 11 presents the residual stress values obtained via neutron diffraction. Figure 11a, b presents the residual stress values for the component produced with the "perimeter first" scan strategy. Figure 11c, d presents the residual stress values for the "edge to edge" scan strategy. Figure 11a, c corresponds to the stresses measured in the outer column location while Fig. 11b, d corresponds to the inner column. Column locations are shown in Fig. 7. Positive values of residual stress are indicative of tensile stresses and negative residual stress values are compressive.

Overall, residual stress measurements ranged between 416 and −290 MPa. Stresses in the x and y directions were found to be predominantly tensile whereas stresses along the z direction were almost exclusively compressive. Stresses observed in the x direction ranged between −74 and 416 MPa, stresses in the y direction ranged between −10 and 303 MPa, and stresses in the z direction ranged between −290 and 45 MPa. In general, x and y directional stresses became
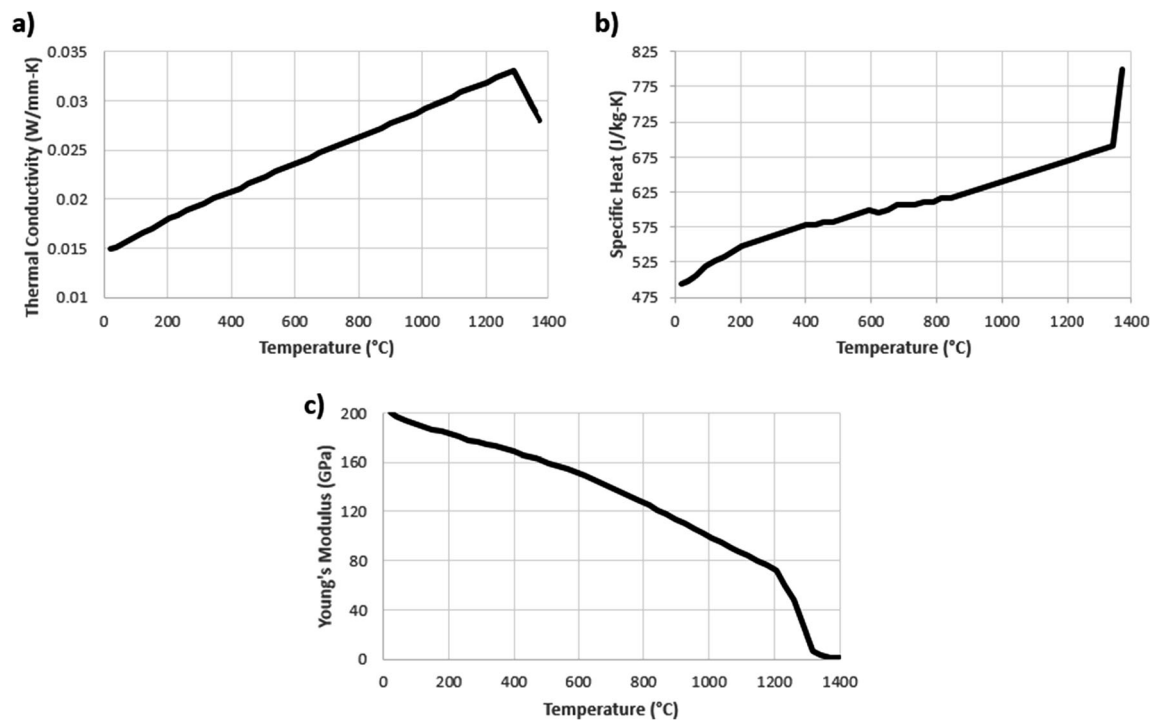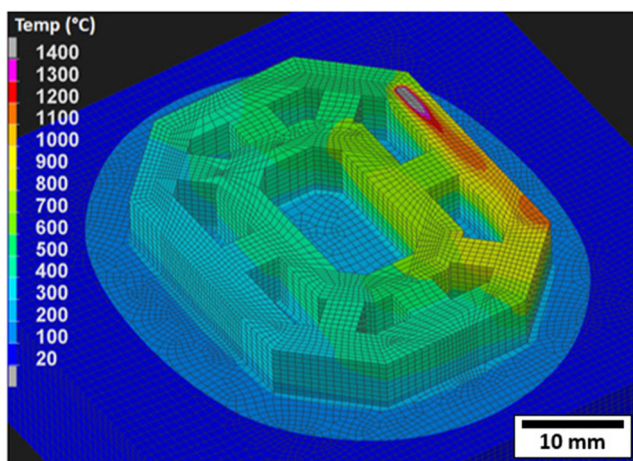
Fig. 9 304L material properties defined as a function of temperature for numerical simulations. **a** Thermal conductivity. **b** Specific heat. **c** Young's modulus

increasingly tensile as the build height increased. Near the bottom of the component, these stresses were relatively non-existent. However, at approximately the middle of the build height (6 mm), the tensile x and y directional stress values began to increase significantly. The extreme case of this increase is shown in Fig. 11b, where the residual stress in the x direction increased 394 MPa over a distance of 3 mm near the top of the build. The maximum x and y stress values were located at the top of each component. In contrast, the opposite case was observed in the z direction, where compressive residual stresses exhibited a decreasing trend as the build height increased. The peak compressive stress values in the z

Fig. 10 Numerical simulation of build procedure using edge to edge scan strategy. Temperature profile shown

direction were observed within the bottom 2 mm of each component. In each case, the compressive stresses became less severe near the top of the components, eventually reaching a value of zero in Fig. 11b, d.

Differences in the residual stress profiles were observed as a function of the laser scan strategy utilized during component production. Primarily, these differences resided in the x and y directional stress values. The component produced with the "perimeter first" scan strategy experienced larger peak residual stress values with respect to the "edge to edge" scan strategy. In the outer column, the x and y directional stress values for the "edge to edge" scan strategy ranged from -50 to 55 MPa. The stresses in this location remained relatively constant throughout the height of the build. However, in the same location for the "perimeter first" scan strategy, the stresses ranged between -74 and 233 MPa while exhibiting a significant increase near the top of the component. Although the stress difference was more pronounced in the outer column, the "perimeter first" scan strategy produced larger residual stresses in the inner column location as well. The x and y directional stress values for the "edge to edge" scan strategy ranged from -3 to 323 MPa. For the "perimeter first" scan strategy, these values ranged between -38 and 416 MPa. Although both components experienced an increase in x and y directional residual stresses as the build height increased, the "perimeter first" scan strategy yielded larger residual stress values.

Although the variation in laser scan strategy produced differences in the x and y directions stress profiles, the z
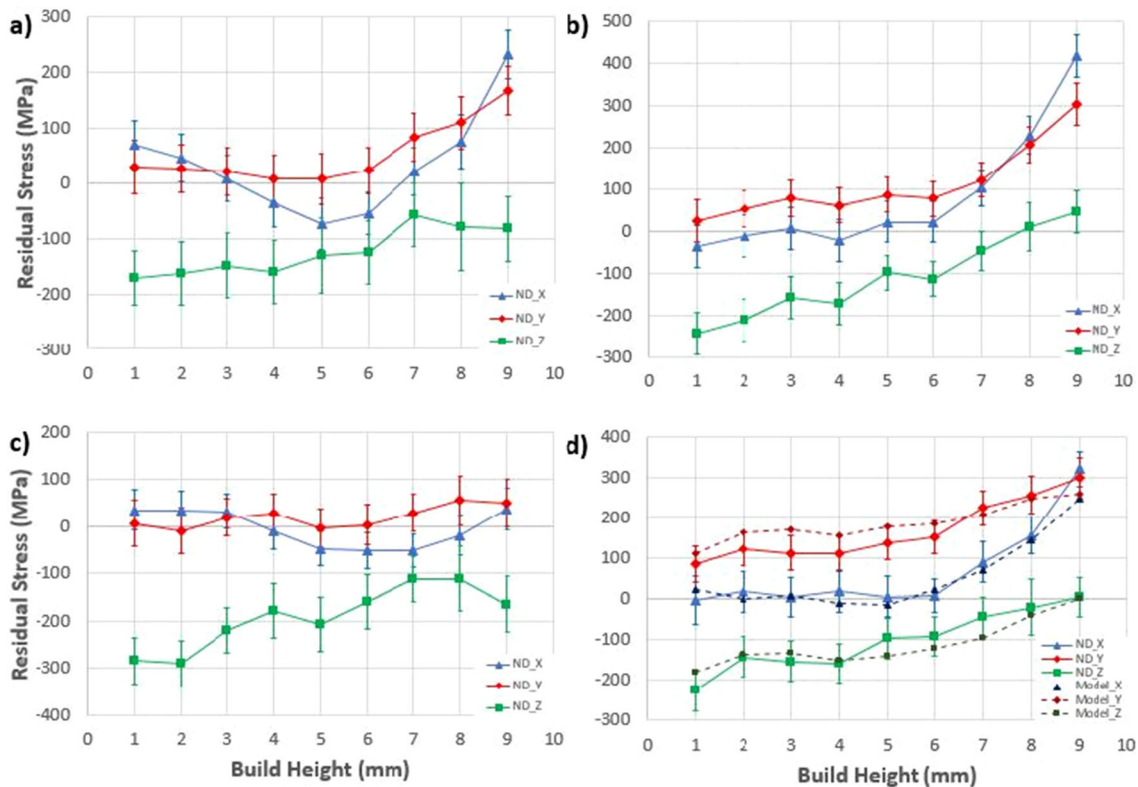
Fig. 11 Neutron diffraction results for **a** "perimeter first" scan strategy, outer column; **b** "perimeter first" scan strategy, inner column; **c** "edge to edge" scan strategy, outer column; and **d** "edge to edge" scan strategy, inner column, in conjunction with numerical simulation results for validation

directional residual stress values were relatively insensitive to the variation in scan strategy. For the "perimeter first" scan strategy, z directional residual stress values ranged between -243 and 45 MPa. For the "edge to edge" scan strategy, the stress values ranged from -225 to 5 MPa. The peak compressive stresses resided near the bottom of each component, and the stress profiles became decreasingly compressive as the build height increased, regardless of the laser scan strategy used. The z directional stresses near the top of the component reached a value of zero for the inner column location of both components.

It should be recognized that the residual stresses measured exhibited drastic changes in value over short distances within the DMLS build. This can be observed when comparing the inner and outer column stress values within the same component at a certain build height. For example, for Fig. 11c, d (outer and inner columns of "edge to edge" scan strategy), at the top of the component, the x directional stresses varied from 37 MPa in the outer column to 323 MPa in the inner column. This is a variation of 286 MPa over a distance of only 3 mm between the inner and outer column locations. Recognizing the potential for significant variations in residual stresses over such a short distance justifies the need for a relatively small gauge volume size, as used in this study. Utilizing a small gauge volume size allows for finer resolution when mapping an area of interest, which will allow for the

detection of significant changes in residual stress over short distances within a DMLS build.

3.2 SYSWELD results

Thermo-mechanical FEA simulations were conducted to model the DMLS build procedure. The simulations were conducted using SYSWELD and the model was validated with experimental neutron diffraction measurements. The purpose of the FEA modeling effort was to develop an accurate tool for evaluating the residual stresses present as a function of additional DMLS process variables. Specifically, this was used to study the influence of build plate preheating on the residual stress profile.

Using the "edge to edge" scan strategy, the simulation residual stress results were plotted in conjunction with neutron diffraction measurements in Fig. 11d. Simulation residual stress values were obtained by selecting nodes within the component which match the locations of the gauge volume measurements. The residual stress values for the selected nodes were then determined after the DMLS build procedure and subsequent cooling to room temperature was complete. As shown in Fig. 11d, the simulation results showed good agreement with the experimental results. In general, the simulated residual stress values resided within the standard errors calculated for the experimental residual stress measurements.

Overall, the range of error between the simulation and experimental results was 5–73 MPa.

Following the model validation, the influence of build plate preheating on the residual stress profile was evaluated. The "edge to edge" scan strategy was utilized, and identical simulations were run with the exception of build plate preheating temperature. Six simulations were run, with build plate preheating temperatures of room temperature, 50, 100, 150, 200, and 250 °C. Upon the completion of each simulation, the z direction residual stress values were plotted as a function of build height. The z direction was selected because residual stresses were found to be consistently prevalent in the z direction in the experimental neutron diffraction results.

Figure 12a presents the simulation results as a function of build plate preheating temperature and Fig. 12b provides an image of the simulation with a build plate preheating temperature of 250 °C. The room temperature residual stress profile of the DMLS build in Fig. 12a is equivalent to the simulated z direction residual stress profile in Fig. 11d. With respect to the room temperature residual stress values, the simulation results exhibited a decrease in the residual stresses present as the build plate preheating temperature increased. A relatively small reduction in stress levels was achieved at the 50 °C preheat temperature. The effect became pronounced as the preheating temperature reached 100 °C. An increase to 150 °C resulted in a reduction of the peak compressive stress value by 58%. The profile of the residual stresses maintained a similar trend as a function of build height until the preheat temperature exceeded 150 °C. Residual stress reductions were further realized as the preheat temperature reached 200 °C. This preheat temperature produced a consistent stress value throughout the height of the build, which was approximately − 10 MPa. At a build plate temperature of 250 °C, residual stress presence was virtually eliminated.

In addition to the residual stresses within the DMLS build, Fig. 12a also presents the residual stresses present in the build plate region. Tensile residual stresses were observed in the build plate, which compensate for the compressive residual stresses within the DMLS build. A peak tensile stress of 148 MPa was observed within the build plate at room temperature. The tensile residual stresses observed within the build plate were reduced as the build plate preheating temperature increased.

3.3 Discussion

Residual stress level was shown to vary as a function of laser scan strategy. The stresses present in the component produced with the "perimeter first" scan strategy were larger than those present from the "edge to edge" scan strategy. As noted previously, this was primarily the case for stresses in the x and y directions whereas z directional stresses were relatively insensitive to laser scan strategy. This behavior can be attributed to a difference in restraint present within the two components. When considering the "perimeter first" scan strategy (Fig. 6a), the connection region is the final area scanned by the laser for each build layer. Thus, the surrounding Block-O regions are built in advance. The presence of the Block-O regions prior to the scanning of the connection region places an increase in restraint at the interface of the two regions. As the connection region cools and material contraction occurs, it is restrained by the surrounding Block-O regions. For the "edge to edge" scan strategy, this restraint is not present. Additionally, the "perimeter first" scan strategy produces material re-melting along the interface of the Block-O and connection regions. This occurs when the laser joins the connection region to the Block-O region. The re-melting and overlap of laser scanning has been shown in previous research to produce increases in residual stresses present for AM builds [35].

Neutron diffraction results also showed a significant increase in x and y directional residual stresses present as the build height increased. In the lower 6 mm of the component, the x and y directional stresses were relatively low. However, in the upper 3 mm of the component, significant increases in the stresses were present. This can be attributed to differences in the overall thermal cycle experienced at different build
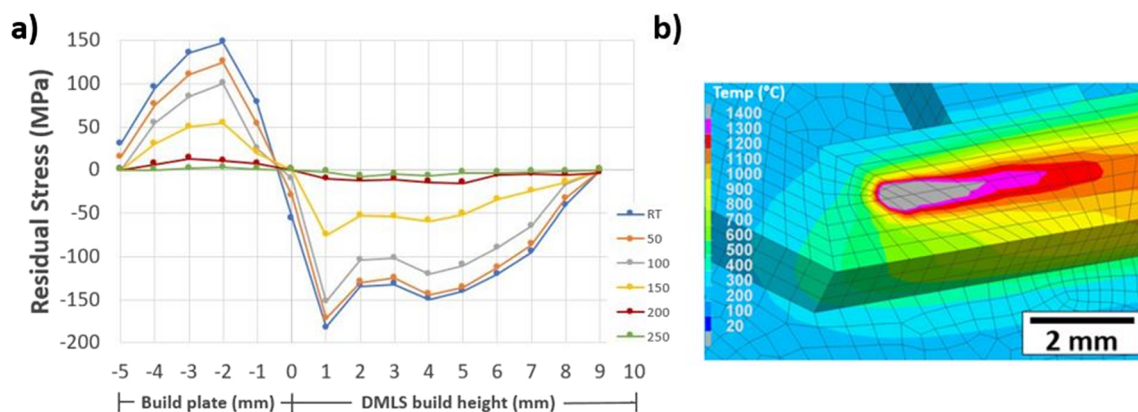
Fig. 12 **a** Numerical simulation results as a function of build plate preheating temperature and **b** numerical simulation image with build plate preheat temperature of 250 °C

heights. The bottom region of the component experiences material reheating when additional build layers are gradually added above. However, the top of the component does not experience the same level of material reheating since additional layers are no longer added above. Similar stress relief behavior has been exhibited in multi-pass welding applications [14]. In effect, this reheating of material in the solid state accomplishes the same purpose as conducting post-processing heat treatments. Therefore, stress relief may be obtainable in the upper regions of the DMLS build by applying additional defocused laser scans. Reheating should be accomplished in the solid state to avoid re-melting of previously deposited material.

It should be recognized that regions of the experimentally measured x and y directional tensile residual stresses exceeded the yield stress of wrought 304L. However, evidence of macroscopic plastic deformation was not observed in these regions. This behavior may be attributed to the improvement of mechanical properties obtained in additively manufactured components [36, 37]. Previous research has reported the yield stress as high as 448 MPa in additively manufactured 304L stainless steel [36–38]. This value, an approximate twofold increase in yield stress with respect to wrought 304L, is achievable due to the Hall-Petch strengthening mechanism associated with grain structure refinement. Due to the rapid melt pool solidification resulting from laser processing, additively manufactured components commonly exhibit refined grain structures with respect to their wrought counterparts. As presented in Fig. 4, the average grain size for the DMLS components evaluated in this study was 21 μm. An additional explanation for this behavior may be attributed to stress triaxiality within the interior of the DMLS components. A triaxial state of stress can lead to the measurement of an individual stress component in excess of the material yield stress, which is measured uniaxially [39, 40]. Although an individual component of residual stress may exceed the yield stress value, triaxiality may prevent plastic deformation from occurring. This has been reported in additional residual stress-related studies [39, 41, 42].

Build plate preheating was shown to virtually eliminate residual stresses present at a preheating temperature of 250 °C. Incremental increases in the preheating temperature up to 250 °C were also shown to partially alleviate the residual stresses present. Build plate preheating is capable of reducing the residual stresses present due to a reduction in the thermal gradient. The surrounding material strength decreases as the temperature is increased, thereby allowing for material expansion and contraction to occur without the same level of restraint as at room temperature. The z directional stresses were evaluated as a function of preheating temperature due to their consistent presence in the experimental DMLS builds.

4 Conclusions

Residual stresses were evaluated for a component produced via DMLS with variations in laser scan strategy. Neutron diffraction was utilized to obtain experimental residual stress measurements. Numerical simulations were developed using FEA to evaluate the influence of build plate preheating on residual stress presence. The following conclusions may be drawn from the results presented:

1) Residual stresses in the x and y directions were predominantly tensile and became increasingly tensile as the build height increased. Stresses in the z direction were predominantly compressive and became decreasingly compressive as the build height increased.

2) Residual stress profiles in the x and y directions were shown to vary as a function of laser scan strategy. This was attributed to differences in restraint present due to the scan strategies imposed. The z directional stresses were relatively insensitive to variations in scan strategy.

3) Measured residual stress values experienced significant variations in value over short distances within the DMLS component. Measurement techniques which offer fine resolution for mapping residual stresses should be employed to ensure detection of significant changes in residual stress.

4) Build plate preheating was proven to be an effective method for reducing the residual stresses present in the DMLS component. This was attributed to a reduction in the thermal gradient present.

References

1. Kranz J, Herzog D (2015) Design guidelines for laser additive manufacturing of lightweight structures in TiAl6V4. J Laser Appl 27:S14001

2. Robbins J, Owen SJ, Clark BW, Voth TE (2016) An efficient and scalable approach for generating topologically optimized cellular structures for additive manufacturing. Additive Manufacturing 12B:296–304

3. Sing SL, An J, Yeong WY, Wiria FE (2015) Laser and electron-beam powder-bed additive manufacturing of metallic implants: a review on processes, materials and designs. J Orthop Res 34: 369–385

4. Hussein A, Hao L, Yan C, Everson R, Young P (2013) Advanced lattice support structures for metal additive manufacturing. J Mater Process Technol 213:1019–1026

5. Thompson S, Aspin Z, Shamsaei N, Elwany A, Bian L (2015) Additive manufacturing of heat exchangers: a case study on a multi-layered Ti-6Al-4V oscillating heat pipe. Addit Manuf 8: 163–174

6. Mellor S, Hao L, Zhang D (2014) Additive manufacturing: a framework for implementation. Int J Prod Econ 149:194–201

7. Dehoff R, Duty C, Peter W, Yamamoto Y, Chen W, Blue C, Tallman C (2013) Case study: additive manufacturing of aerospace brackets. Adv Mater Process 171:19–22

8. Gibson I, Rosen D, Stucker B (2015) Additive manufacturing technologies: 3D printing, rapid prototyping, and direct digital manufacturing, Second edn. Springer, New York City

9. W.J. Sames, F.A. List, S. Pannala, R.R. Dehoff, S.S. Babu, The metallurgy and processing science of metal additive manufacturing, Int Mater Rev

10. Mercelis P, Kruth JP (2006) Residual stresses in selective laser sintering and selective laser melting. Rapid Prototyp J 12:254–265

11. Zaeh M, Branner G (2010) Investigations on residual stresses and deformations in selective laser melting. Prod Eng 4:35–45

12. Pohl H, Simchi A, Issa M, Dias H (2001) Thermal stresses in direct metal laser sintering. Proceedings of the Solid Freeform Fabrication Symposium:366–372

13. Siddique S, Imran M, Wycisk E, Emmelmann C, Walther F (2015) Influence of process-induced microstructure and imperfections on mechanical properties of AlSi12 processed by selective laser melting. J Mater Process Technol 221:205–213

14. Lippold JC (2015) Welding metallurgy and weldability. John Wiley & Sons, Inc, Hoboken

15. Totten G (2002) Handbook of residual stress and deformation of steel. ASM International, Materials Park, OH

16. Hutchings MT, Withers PJ, Holden TM, Lorentzen T (2005) Introduction to the characterization of residual stress by neutron diffraction. Taylor & Francis Group, Boca Raton, Florida

17. Zhao X, Iyer A, Promoppatum P, Yao SC (2017) Numerical modeling of the thermal behavior and residual stress in the direct metal laser sintering process of titanium alloy products. Additive Manufacturing 14:126–136

18. Shiomi M, Osakada K, Nakamura K, Yamashita T, Abe F (2004) Residual stress within metallic model made by selective laser melting process. CIRP Ann 53:195–198

19. Sochalski-Kolbus L, Payzant EA, Cornwell PA, Watkins TR, Babu SS, Dehoff RR, Lorenz M, Ovchinnikova O, Duty C (2015) Comparison of residual stresses in Inconel 718 simple parts made by electron beam melting and direct laser metal sintering. Metall Mater Trans A 46:1419–1432

20. A.E. Patterson, S.L. Messimer, P.A. Farrington (2017) Overhanging features and the SLM/DMLS residual stresses problem: review and future research need, Technologies, 5

21. Teng T, Lin C (1998) Effect of welding conditions on residual stresses due to butt welds. Int J Press Vessel Pip 75:857–864

22. Adedayo SM, Adeyemi MB (2000) Effect of preheat on residual stress distributions in arc-welded mild steel plates. J Mater Eng Perform 9:7–11

23. Slotwinski J, Garboczi E, Stutzman P, Ferraris C, Watson S, Peltz M (2014) Characterization of metal powders used for additive manufacturing. J Res NIST 119:460–493

24. Standard guide for preparation of metallographic specimens, ASTM E3-11, American Society for Testing and Materials, West Conshohocken, PA. (2017)

25. Standard practice for determining the inclusion or second-phase constituent content of metals by automatic image analysis, ASTM E1245-03, American Society for Testing and Materials, West Conshohocken, PA., in, 2016

26. S. Spooner, X. Wang, Diffraction peak displacement in residual stress samples due to partial burial of the sampling volume, 30 (1997) 449–455

27. Wang X, Spooner S, Hubbard C (1998) Theory of the peak shift anomaly due to partial burial of the sampling volume in neutron diffraction residual stress measurements. J Appl Crystallogr 31:52–59

28. Preuss M, Withers PJ, Pang JWL, Baxter GJ (2002) Inertia welding nickel-based superalloy: part II. Residual stress characterization. Metall Mater Trans A 33:3227–3234

29. Iqbal N, Rolph J, Moat R, Hughes D, Hofmann M, Kelleher J, Baxter G, Withers PJ, Preuss M (2011) A comparison of residual stress development in inertia friction welded fine grain and coarse grain nickel-base superalloy. Metall Mater Trans A 42:4056–4063

30. Krawitz AD, Winholtz RA (1994) Use of position-dependent stress-free standards for diffraction stress measurements. Mater Sci Eng A 185:123–130

31. Wang XL, Payzant EA, Taljat B, Hubbard CR, Keiser JR, Jerinec MJ (1997) Experimental determination of the residual stress in a spiral weld overlay tube. Mater Sci Eng A 232:31–38

32. Webster PJ, Mills G, Wang XD, Kang WP, Holden TM (1995) Neutron strain scanning of a small welded austenitic stainless steel plate. J Strain Anal Eng Des 30:35–43

33. Cai Z, Zhao H (2013) Efficient finite element approach for modelling of actual welded structures. Sci Technol Weld Join 8:195–204

34. Kruth JP, Wang X, Laoui T, Froyen L (2003) Lasers and materials in selective laser sintering. Assem Autom 23:357–371

35. Liu F, Lin X, Yang G, Song M, Chen J, Huang W (2011) Microstructure and residual stress of laser rapid formed Inconel 718 nickel-base superalloy. Opt Laser Technol 43:208–213

36. Brown B, Everhart W, Dinardo J (2016) Characterization of bulk to thin wall mechanical response transition in powder bed AM. Rapid Prototyp J 22:801–809

37. S. Karnati, I. Axelsen, F.F. Liou, J.W. Newkirk (2016) Investigation of tensile properties of bulk and SLM fabricated 304L stainless steel using various gage length specimens, Proceedings of the Solid Freeform Fabrication Symposium, 592–604

38. D. Gill, J. Smugeresky, C. Atwood (2006) Repeatability analysis of 304L deposition by the LENS process, Proceedings of the Solid Freeform Fabrication Symposium, 770–776

39. Robinson JS, Tanner DA, Truman CE (2014) 50th anniversary article: the origin and management of residual stress in heat-treatable aluminum alloys. Strain 50:185–207

40. Prime MB, Gnaupel-Herold T, Baumann JA, Lederich RJ, Bowden DM, Sebring RJ (2006) Residual stress measurements in a thick, dissimilar aluminum alloy friction stir weld. Acta Mater 54:4013–4021

41. Prime MB, Sebring RJ, Edwards JM, Hughes DJ, Webster PJ (2004) Laser surface-contouring and spline data smoothing for residual stress measurement. Exp Mech 44:176–184

42. Webster GA, Ezeilo AN (2001) Residual stress distributions and their influence on fatigue lifetimes. Int J Fatigue 23:375–383

43. ESI-Group. SYSWELD V12.0 reference manual., (2017)